ISPRS Journal of Photogrammetry and Remote Sensing 169 (2020) 152–165

Contents lists available at ScienceDirect

ISPRS Journal of Photogrammetry and Remote Sensing

journal homepage: www.elsevier.com/locate/isprsjprs

Effects of radiometric correction on cover type and spatial resolution for modeling plot level forest attributes using multispectral airborne LiDAR data

Wai Yeung Yan [a,b,*], Karin van Ewijk [c], Paul Treitz [c], Ahmed Shaker [b]

[a] Department of Land Surveying and Geo-Informatics, The Hong Kong Polytechnic University, Hung Hom, Kowloon, Hong Kong
[b] Department of Civil Engineering, Ryerson University, Toronto, Ontario, Canada
[c] Department of Geography and Planning, Queen's University, Kingston, Ontario, Canada

ARTICLE INFO

Keywords:
Multispectral LiDAR
LiDAR scan line correction
Overlap-driven intensity correction
Intensity banding
Forest attributes
Area-based approach
Random forests

ABSTRACT

In order to use the airborne LiDAR intensity in conjunction with the height-derived information for forest modeling and classification purposes, radiometric correction is deemed to be a critical pre-processing requirement. In this study, we implemented a LiDAR scan line correction (LSLC) and an overlap-driven intensity correction (OIC) to remove the stripe artifacts that appeared within the individual flight lines and overlapping regions of adjacent flight lines of a multispectral LiDAR dataset. We tested the effectiveness of these corrections in various land/forest cover types in a temperate mixed mature forest in Ontario, Canada. Subsequently, we predicted three plot level forest attributes, i.e., basal area (BA), quadratic mean diameter (QMD), and trees per hectare (TPH), using different combinations of height and intensity metrics derived from the multispectral LiDAR data to determine if LiDAR intensity data (corrected and uncorrected) improved predictions over models that utilize LiDAR height-derived information only. The results show that LSLC can reduce the intensity banding effect by 0.19–23.06% in channel 1 (1550 nm) and 4.79–66.87% in channel 2 (1064 nm) at the close-to-nadir region. The combined effect of LSLC and OIC is notable particularly at the swath edges. After implementing both methods, the intensity homogeneity is improved by 5.51–12% in channel 1, 6.37–42.93% in channel 2, and 6.48–33.77% in channel 3 (532 nm). Our results further demonstrate that BA and QMD predictions in our study area gained little from additional LiDAR intensity metrics. Intensity metrics from multiple LiDAR channels and intensity normalized difference vegetation index (NDVI) metrics did improve TPH predictions up to 7.2% in RMSE and 1.8% in Bias. However, our lowest TPH prediction errors (%RMSE) were still approximately 10% larger than for BA and QMD. We observed only minimal differences in plot level BA, QMD, and TPH predictions between models using original and corrected intensity. We attribute this to: (i) the lower effectiveness of radiometric correction in forest versus grassland, bare soil and road land cover types, and (ii) the effect of spatial resolution on intensity noise.

1. Introduction

Over the last decade, airborne LiDAR data have proven to be valuable for supporting a range of forest monitoring and sustainable forest management applications at a variety of spatial scales (Wulder et al., 2013). These spatially-explicit predictions of forest ecosystem attributes can be derived from airborne LiDAR data only (Lefsky et al., 1999; Næsset et al., 2004; Ørka et al., 2009; Im et al., 2008) or in combination with optical remote sensing data (Kandare et al., 2017; Dalponte et al., 2012; Guo et al., 2011). The attributes of interest in these forest ecosystems range from individual tree attributes (e.g., tree species, tree diameter and crown) using individual tree crown (ITC) approaches (Budei et al., 2018; Axelsson et al., 2018), and plot level attributes (e.g., canopy height, crown closure, biomass, timber volume, leaf area index (LAI), stem density, forest health) using area-based approaches (ABA) (Wulder et al., 2013; Næsset, 2007), to classification of forest cover types (e.g., natural forests, plantations, bare soils, grassland, shrubland and roads) (Hopkinson et al., 2016) and habitats (Vierling et al., 2008).

The height/geometry contained within the LiDAR data provides detailed information on the three-dimensional structure of forests (Lim

* Corresponding author at: Department of Land Surveying and Geo-Informatics, The Hong Kong Polytechnic University, Hung Hom, Kowloon, Hong Kong.
E-mail addresses: waiyeung.yan@polyu.edu.hk, waiyeung.yan@ryerson.ca (W.Y. Yan).

https://doi.org/10.1016/j.isprsjprs.2020.09.001
Received 23 April 2020; Received in revised form 26 August 2020; Accepted 1 September 2020
Available online 22 September 2020

et al., 2003), whereas the backscattering properties of the laser signal strength within the LiDAR data potentially offers the ability to discriminate between different land cover types, tree species, and their canopy elements based on how the peak laser energy is backscattered from the different features (Yan and Shaker, 2014; Hopkinson et al., 2016). Until recently, most studies predicting these forest attributes were performed using monochromatic LiDAR sensors operating at wavelengths of 1064 nm or 1550 nm. However, since 2015, a multispectral LiDAR sensor has become commercially available. The Optech Titan (Teledyne Optech, Vaughan, Ontario, Canada) consists of three laser channels with wavelengths of 1550 nm, 1064 nm, and 532 nm, enabling the use of structural and backscattering properties from three different channels, rather than one, and the generation of band ratios and vegetation indices (Morsdorf et al., 2009) for the prediction of forest attributes.

In terms of individual tree species classification, several studies have shown that the height distribution, geometric/shape, and/or intensity features extracted from monochromatic LiDAR data have been reasonably successful for distinguishing between conifers and broadleaved species and the classification of a low number of tree species (Ørka et al., 2009; Korpela et al., 2010). However, the limited spectral information in monochromatic LiDAR systems has been challenging for tree species classification when a larger number of species are involved (Brandtberg, 2007; Kim et al., 2011). More recent studies, using multispectral Titan data, have reported improved tree species classification compared to classifications performed with monochromatic LiDAR data (Axelsson et al., 2018; Budei et al., 2018; Yu et al., 2017).

Most studies that predict plot level forest attributes using the ABA approach have predominantly used height-derived information from monochromatic LiDAR data. However, some studies have incorporated LiDAR intensity variables to improve the estimation of biomass carbon stock (García et al., 2010), diameter distribution models (Shang et al., 2017), and gap fraction (Hopkinson and Chasmer, 2009) where they assumed that intensity metrics may capture differences among tree species, characterize foliage distribution within the canopy (Morsdorf et al., 2010), and capture the crown permeability and canopy layering (Shang et al., 2017). To date, only a few studies have predicted plot/stand level attributes (Dalponte et al., 2018; Kukkonen et al., 2019a; Kukkonen et al., 2019b) using multispectral LiDAR data. For example, Dalponte et al. (2018) showed that regression models using multispectral LiDAR height and intensity metrics resulted in more accurate above ground biomass, diameter variability, tree species diversity, and stem density predictions compared to models using metrics derived from monochromatic LiDAR in Southern Norway. In particular, metrics derived from the 1550 nm channel seemed useful for the prediction of these forest attributes (Dalponte et al., 2018). Kukkonen et al. (2019a) compared dominant species and species composition predictions derived from multispectral and monochromatic LiDAR data (and in combination with aerial imagery) for a managed boreal forest in Eastern Finland. Their findings suggest that multispectral LiDAR provided similar information to that found in the combination of monochromatic LiDAR data and aerial imagery for the prediction of dominant tree species and discrimination between conifer and broadleaved tree species (Kukkonen et al., 2019a). However, Kukkonen et al. (2019b) also reported that the predictive performance of species-specific volume models with multispectral LiDAR data alone was not as good as monochromatic or multispectral LiDAR data in combination with aerial images. In addition, the Scandinavian biome includes three dominant tree species (two conifer and one broadleaved tree species) with distinct spectral signatures. In our biome that includes a larger number of dominant species, the findings of Kukkonen et al. (2019a,b) may not hold. 3D point cloud data collected by airborne LiDAR systems equipped with single or multiple laser channel(s) have been used for land cover classification. Many of these studies showed the advantage of the height/geometry contained within the LiDAR data for land-cover classification because of its ability to, for example, recognize building and road features (Zhang et al., 2006), distinguish high and low vegetation (Charaniya et al., 2004), and grassland and shrubland (Chen et al., 2009). Other studies have shown the benefit of LiDAR intensity data to separate various land cover types. For example, Charaniya et al. (2004) used LiDAR intensity data to distinguish between roads and low vegetation. For a review on urban land classification using monochromatic LiDAR data, see Yan et al. (2015). Recent studies have investigated the utility of multispectral LiDAR data, i.e., the Optech Titan, to classify land cover types (Bakuła et al., 2016; Hopkinson et al., 2016; Matikainen et al., 2017). For example, Matikainen et al. (2017) showed that multispectral intensity metrics from multiple channels were more useful for the classification of built-up, trees, asphalt, gravel, rocky areas, and low vegetation cover types than those based on a single LiDAR channel. Bakuła et al. (2016) reported an overall accuracy over 90% for a classification of six land cover types in Toronto, Ontario, Canada, using information derived from multispectral intensity and height data. For more examples of land cover classification studies performed with the multispectral Titan data, see Matikainen et al. (2017), Morsy et al. (2017).

In order to use the LiDAR intensity for forest modeling and classification purposes, radiometric calibration, correction, and normalization of LiDAR data are deemed to be a critical pre-processing step to improve the quality of the intensity/waveform data. Due to the unique characteristics of how LiDAR data are collected, the backscattered laser signal strength depends on various factors, including the range, scan angle, atmospheric condition, surface topography (and roughness), and other not readily available values of some system parameters, such as emitted laser power, aperture size, gain control, and system transmission factor. As a result, most of the existing calibration, correction, and normalization models are built upon the radar (range) equation with a consideration of the above-mentioned parameters. A number of studies have successfully demonstrated the impact of these models on improving the analytical capability toward different applications. Korpela et al. (2010) conducted a range and gain control normalization where an improvement of tree species classification was found ranging from 6% to 9%. Yan and Shaker (2014) recorded an improvement of 5.7% to 16.5% in overall accuracy for an urban land-cover classification after implementing both radiometric correction and normalization on Leica ALS-50 LiDAR data. Despite all these successful attempts, there still exist several research voids that require further examination.

First, some of the existing experiments deal with individual LiDAR flight lines only, where the correction model can be directly implemented (Hopkinson, 2007). However, stripe artifacts may occur while combining multiple overlapping flight lines even after radiometric correction. This is mainly caused when the strongly attenuated laser signals found at the swath edges of a data strip is combined with another data strip with less attenuated laser signals at the close-to-nadir region. Second, even though solutions of normalization of multiple flight lines are proposed, they require users to define the correction model parameters. Existing correction or normalization models such as Korpela et al. (2010) and Gatziolis (2011) require users to define the model parameters to adjust the degree of correction for the range for each laser pulse. Kukkonen et al. (2019a) investigated the optimal model parameter of the (range only) intensity correction for multispectral airborne LiDAR data, and suggested that the value of the correction parameter for the respective three laser channels was less than what the existing literature suggested (i.e., two). Since the definition of these parameters depends on the LiDAR sensor as well as the studied environment, the correction parameters vary in different scenarios. To overcome such a drawback, a correction model that is capable of handling monochromatic and multispectral LiDAR intensity data should be introduced without the need for manual intervention.

The purpose of this paper is twofold. First, we assessed the implementation of a LiDAR scan line correction (LSLC) and an overlap-driven intensity correction (OIC), respectively, to remove stripe artifacts that appeared in both individual flight lines and overlapping regions of the

multispectral LiDAR data. Second, we assessed the potential of predicting forest attributes at the plot level using the multispectral LiDAR data.

We aim to answer the following questions:

1. What is the effectiveness of LSLC and OIC for removing/reducing stripe artifacts within different regions of the LiDAR flight lines?
2. Are LiDAR intensity values within different forest cover types affected differently by LSLC and OIC?
3. Does the inclusion of multispectral LiDAR intensity significantly improve predictions of plot level forest attribute models (i.e., for basal area (BA), quadratic mean diameter (QMD), and trees per hectare (TPH)) over models that utilize LiDAR normalized height information only?
4. What is the effect of LSLC and OIC on the prediction of the plot level forest attributes?

2. Material and methods

2.1. Study area

The Petawawa Research Forest (PRF-site) (45°57′N, 77°34′W; approximately 350 m above mean sea level) covers approximately 10,000 ha and is located within the Great Lakes Saint Lawrence forest region of Ontario, Canada (Fig. 1). The PRF-site is a mixed mature forest and includes both managed and unmanaged forest stands. Managed stands include plantations consisting of a variety of tree species and various initial planting densities and silvicultural treatments (e.g., a uniform shelterwood system) (Woods et al., 2008). The dominant species in the PRF-site include eastern white (*Pinus strobus* L.), red (*Pinus resinosa* Ait.) and jack pine (*Pinus banksiana* L.), trembling aspen (*Populus tremuloides* Michx), white birch (*Betula papirifera* Marsh.), and tolerant hardwood species, such as red maple (*Acer rubrum* L.) and sugar maple (*Acer saccharum* Marsh). The pine species are predominantly found on dry nutrient-poor sites whereas the intolerant and tolerant hardwoods are found on respectively sandy to clayey upland sites and nutrient-rich uplands. Shade-tolerant conifers such as eastern hemlock (*Tsuga canadensis* L.) and Red oak (*Quercus rubra* L.) have relatively lower abundances in the PRF-site (Carleton, 2003; Watkins, 2011).

2.2. Airborne data collection

A total of 33 multispectral LiDAR flight lines were collected during the growing season (i.e., during leaf-on conditions) for the PRF-site on July 20, 2016 (Fig. 1). Prior to, and during the data acquisition there was no precipitation and the average air temperature was 20°C (PRF-site weather station). It took approximately three hours to complete the LiDAR data acquisition. In each of the flight lines, three sets of airborne LiDAR point clouds corresponding to the three laser channels (i.e., channel 1 = 1550 nm, channel 2 = 1064 nm, and channel 3 = 532 nm) were collected by an Optech Titan sensor (Teledyne Optech, Vaughan, ON, Canada). The flying height of the airborne survey was approximately 1.1 km, and each flight line has an approximate 50% overlap with adjacent flight lines. The pulse repetition frequency and the scan frequency are 375 kHz and 40 Hz, respectively. Although the elevation accuracy and precision of Optech Titan are survey specific, they are in general less than 10 cm and 2 cm, respectively (Fernandez-Diaz et al., 2016). A more detailed description of the Titan multispectral LiDAR sensor can be found in Fernandez-Diaz et al. (2016). The acquired LiDAR data were not range-normalized by the data provider or the sensor manufacturer. The flight and data specifications are outlined in Table 1.

2.3. Field data collection

Field data were collected in the weeks around the airborne LiDAR data acquisition (July 2016) and the following year in June-July 2017. Field plot selection was based on a network of previously established field plots that used a stratified random sampling design (Penner and Woods, 2015). Circular plots were established in forest stands that had an average tree height ⩾5 m, included the majority of the forest types present in the PRF-site and covered a range of BA conditions. All field plot centers were geo-referenced using a SX Blue II-GNSS survey grade GPS unit (Table 2). The field data included information on tree species, current status (alive or dead), and diameter at breast height (DBH at ~ 1.3 m). This information was collected for all trees over a DBH threshold

Table 1
Airborne LiDAR sensor specifications.

Parameter	Specification
Sensor	Optech Titan
Acquisition date	July 20, 2016
Wavelengths	1550 nm (channel 1) 1064 nm (channel 2) 532 nm (channel 3)
Pulse repetition frequency	375 kHz (combined)
Scan frequency	40 Hz
Scan half angle	20°
Flying height	1.1 km AGL
Overlap	50%
Average point density	11.9 pts/m^2 (channel 1) 12.4 pts/m^2 (channel 2) 4.8 pts/m^2 (channel 3)

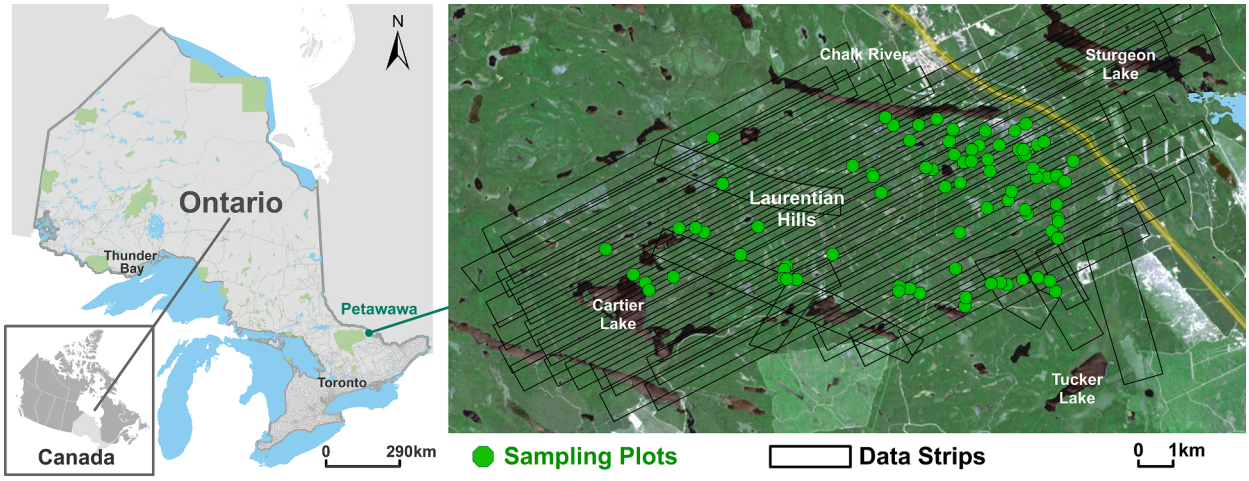

Fig. 1. Study area and location of the 84 sampling plots.

Table 2
Field data specifications.

Parameter	Specification
Data collection	2016, 2017 (June–July)
Number of plots	84
Plot size (m^2)	1000
DBH threshold (cm)	9
GPS unit	SX Blue II-GNSS
(listed accuracy)	(2drms = sub-60 cm, 95% confidence)

of 9 cm. A summary of the field data is presented in Table 3.

3. Method

The entire data processing workflow is summarized in Fig. 2. The multispectral airborne LiDAR data had notable levels of stripe artifacts, which was found in some of the individual flight lines and overlapping regions. It was therefore necessary to first reduce the stripe artifacts found in individual flight lines by implementing the LSLC. This process is optional and was only applied when a specific data channel suffered from intensity banding. Second we applied an OIC to the overlapping flight lines to reduce the stripe artifacts that can be particularly serious at swath edges. After removing the stripe artifacts, the LiDAR intensity data (original and corrected) together with the height attributes derived from the LiDAR data were used to build five different non-parametric (i.e., random forest) predictive models per forest attribute (BA, QMD, and TPH) at the study site. We then tested whether BA, QMD, and TPH predictions in the PRF-site improved with additional LiDAR intensity metrics and whether model performance changed with the improved radiometric quality of the multispectral LiDAR intensity data. We assessed the performance of these models using %RMSE and %Bias and tested the equivalence of the predictions with observed values of the forest attributes using regression-based equivalence tests (Robinson and Froese, 2004; Robinson et al., 2005).

3.1. LiDAR scan line correction (LSLC)

The LSLC is an optional process to be implemented when an individual LiDAR flight line has notable stripe artifacts, which is mainly found in LiDAR systems operated with an oscillating mirror. Such stripe artifacts can be attributed to the intensity banding effect, which is caused by the backscattered laser pulses partially falling outside the receiver's field of view in a particular scanning direction. As a result, the recorded backscattered laser energy at this particular scanning direction is consistently lower than that of the opposite one. To resolve this issue, the LSLC proposed by Yan and Shaker (2018) can be implemented to reduce the intensity banding effect. The LSLC includes the following steps:

1. Split the LiDAR flight line into two subsets based on the scanning direction;
2. Pair up the unique returns of data points from these two subsets based on the nearest distance and a cut-off distance (i.e., the mean point spacing);
3. Create a joint histogram using the paired intensity data points from the two subsets;
4. Establish a correction function (i.e., a polynomial model) that includes both intensity and scan angle based on a robust regression;
5. Perform the correction on the intensity data of the subset, which has consistently lower intensity values (based on the average mean intensity value of the two opposite scan lines), using the estimated model parameters; and
6. Combine the two subsets to form the LSLC intensity flight line.

Details of LSLC can be found in Yan and Shaker (2018). In this study, we only implemented the LSLC to those LiDAR flight lines that showed significant amount of stripe artifacts, which are channel 1 (1550 nm) and channel 2 (1064 nm). After implementing the LSLC, the LiDAR intensity data should undergo the following OIC in order to adjust the effects of range, angle, and atmospheric attenuation.

Table 3
Field data summaries for all sample plots ($n = 84$).

Forest attribute	Mean (Standard deviation)	Minimum	Maximum
Basal area (BA) (m^2 ha^{-1})	29.3 (11.1)	5.2	64
Quadratic mean diameter (QMD) (cm)	22.6 (7.9)	9.8	49.8
Trees per hectare (TPH) (stems ha^{-1})	881 (429)	317	1384

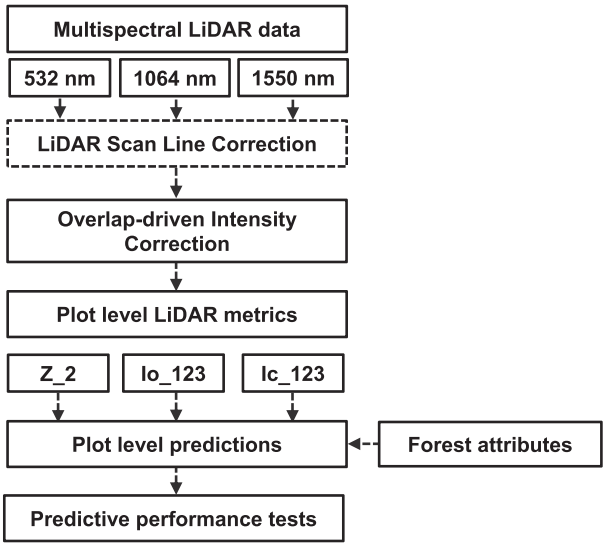

Fig. 2. Overall data processing workflow. The three groups of plot level LiDAR metrics are: normalized height-based metrics from channel 2 (Z_2), uncorrected intensity metrics from channels 1, 2 and 3 (Io_123), and corrected intensity metrics from channels 1, 2 and 3 (Ic_123).

3.2. Overlap-driven intensity correction (OIC)

Most of the existing radiometric correction and normalization approaches are built upon the radar (range) equation, which describes the relationship between the emitted laser power (P_t) and the backscattered laser signal strength (P_r), depending on a number of system and environmental parameters (Jelalian, 1992). The radar (range) equation is listed as below:

$$P_r = \frac{P_t D_r^2}{4\pi R^4 \beta_t} \eta_{atm} \eta_{sys} \sigma \quad (1)$$

where D_r is the aperture diameter, R is the range, β_t is the laser beam width, η_{sys} and η_{atm} are the system transmission factor and atmospheric attenuation, respectively, and finally σ describes the characteristics of the laser pulse being backscattered from the ground objects:

$$\sigma = 4\pi\rho A \cos\theta \quad (2)$$

where ρ refers to the relative (or pseudo) reflectance of the surface, A is the projected laser footprint, and θ refers to the angle of incidence. The atmospheric attenuation factor η_{atm} can be modeled as follows:

$$\eta_{atm} = e^{-2\tau R} \quad (3)$$

where τ represents the sum of the absorption and scattering coefficients from the aerosol and molecular particles. Most of the current correction approaches assume that a diffuse reflectance occurs on any impenetrable surface. Therefore, the cosine of incidence angle can be used to describe the diffuse reflectance. The system factor η_{sys} has been handled by the LSLC with respect to the banding effect. Therefore, this parameter is being ignored in the OIC. Since the parameters P_t, β_t, and D_r can be assumed as unchanged or stable during the survey mission, the correction model can be written as:

$$I_c = \rho \propto I \cdot \frac{R^2}{\cos\theta} \cdot e^{2\tau R} \tag{4}$$

where I_c is the corrected (or normalized) LiDAR intensity value and I is the original LiDAR intensity value. The above equation is used for radiometric calibration/correction by normalizing the data with the square of a reference range found in the LiDAR data strip (e.g., flying height or minimum range ($R_{\min}$)), and often applied in forestry and vegetation studies (Hopkinson, 2007; Yu et al., 2017).

The above model is generally applied to a single airborne LiDAR flight line. Regarding overlapping LiDAR flight lines, existing studies have investigated different correction parameters to feed in the above mentioned model so as to minimize the radiometric discrepancy between the overlapping flight lines (Korpela et al., 2010; Gatziolis, 2011). However, these pre-defined parameters are system and site dependent. As a result, we propose an OIC model based on the framework of Gatziolis (2011) and Ding et al. (2013). Reformulate Eq. (1) by substituting other parameters from Eqs. (2) and (3):

$$I_c = I \cdot \left[\frac{R}{R_{\min}}\right] \cdot \frac{1}{\cos\theta} \cdot e^{2\tau R} \tag{5}$$

Eq. (5) is based on the assumption of diffuse reflectance, where such a setting can only handle homogeneous landscape and stable LiDAR system settings. Recent studies further explore the application of different bidirectional reflectance distribution functions (BRDF), such as the Phong (Tan and Cheng, 2017; Ding et al., 2013; Jutzi and Gross, 2010) or the Torrance-Sparrow reflectance model (Poullain et al., 2016). Some of these BRDFs apply the higher order cosine law or use the polynomial approximation of the range effect (Höfle and Pfeifer, 2007). As a result, Eq. (5) can be re-written as:

$$I_c = I \cdot \left[\frac{R}{R_{\min}}\right]^a \cdot \left[\frac{1}{\cos\theta}\right]^b \cdot e^{2cR} \tag{6}$$

Unless different calibration targets are available during the survey, the correction parameters a, b and c cannot be estimated. Therefore, we use overlapping flight lines to estimate the correction parameters by first pairing up the closest data points from the overlapping flight lines. Assuming no gain control is implemented, the corrected intensity, i.e., relative (or pseudo) reflectance, consider to be identical.

$$\frac{I_{c_i}}{I_{c_j}} = \left[I_i \cdot \left[\frac{R_i}{R_{min}}\right]^a \cdot \left[\frac{1}{\cos\theta_i}\right]^b \cdot e^{2cR_i}\right] \Big/ \left[I_j \cdot \left[\frac{R_j}{R_{min}}\right]^a \cdot \left[\frac{1}{\cos\theta_j}\right]^b \cdot e^{2cR_j}\right] \tag{7}$$

We assume the first return of the paired closest points represent the same object surface, i.e., $I_{c_i} = I_{c_j}$. In this case, Eq. (7) can be reformulated as:

$$\frac{I_i}{I_j} = \left[\frac{R_j}{R_i}\right]^a \cdot \left[\frac{\cos\theta_i}{\cos\theta_j}\right]^b \cdot e^{2(R_j - R_i)c} \tag{8}$$

Given the above equation is in a non-linear form, we apply a logarithm to the equation in order to solve the correction parameters:

$$\ln\left[\frac{I_i}{I_j}\right] = a \cdot \ln\left[\frac{R_j}{R_i}\right] + b \cdot \ln\left[\frac{\cos\theta_i}{\cos\theta_j}\right] + 2(R_j - R_i)c \tag{9}$$

In matrix form, the linearized equation can be represented as:

$$\begin{bmatrix} \ln\left[\frac{R_j}{R_i}\right] & \ln\left[\frac{\cos\theta_i}{\cos\theta_j}\right] & 2[R_j - R_i] \end{bmatrix} \cdot \begin{bmatrix} a \\ b \\ c \end{bmatrix} = \ln\left[\frac{I_i}{I_j}\right] \tag{10}$$

where it can be formulated as:

$$\mathbf{AX} = \mathbf{L} \tag{11}$$

To solve the correction parameters X, an ordinary least squares is applied:

$$\mathbf{X} = (\mathbf{A}^\top \mathbf{A})^{-1} \mathbf{A}^\top \mathbf{L} \tag{12}$$

If multiple LiDAR data strips are acquired, the above-mentioned process should pair up data points from different overlapping data strips in order to estimate a set of universal correction parameters. Once the correction parameters (a, b and c) are solved, they are applied to Eq. (6) to perform the radiometric correction. To further improve the robustness of the solution, we employed a M-estimator to handle potential outliers during the least-squares adjustment. In practice, the OIC should be implemented on the LiDAR data points so that the radiometric discrepancy found in the overlapping region can be reduced. Such a step is important for fine-scale seamless LiDAR-based land cover classification and wall-to-wall LiDAR-based predictions of ITC and ABA tree and forest attributes. However, it is possible to conduct the radiometric correction only on the spatial extents of the sample plots by combining all the overlapping LiDAR intensity data of the sample plots. This way, the computational time can be significantly reduced.

3.3. Multispectral airborne LiDAR data processing for plot-level forest attribute predictions

Prior to extracting the multispectral LiDAR metrics, we height-normalized the LiDAR data using ground returns from a previous LiDAR (i.e., 2012) data acquisition over the PRF-site. Trend analysis results comparing the two LiDAR acquisitions indicated that there was no significant trend of elevation difference ($\alpha = 0.05$), and an elevation translation of 0.79 m was applied to the previous (i.e., 2012) LiDAR data to match the 2016 LiDAR data acquisition. For each plot, we extracted multispectral LiDAR metrics, which we divided into two main types: (1) normalized height-based metrics (from channel 2 only), and (2) intensity-based metrics (from channels 1, 2 and 3) (Table 4). The first type of metrics included measures of central tendency, measures of dispersion, height percentiles, canopy cover/density, and stand complexity metrics based on LiDAR normalized height (z) values. For this group of metrics, we used all returns without filtering the point clouds based on any height threshold. The latter was based on the results of Woods et al. (2008), Woods et al. (2011) who concluded that forest attribute models created using LiDAR metrics without a height threshold performed better than those models filtered with a height threshold. The second group included LiDAR intensity metrics, using first returns only, consisting of measures of central tendency, dispersion and cumulated intensity at height percentiles extracted from each of the three channels. We also included three normalized difference vegetation indices (NDVI) computed by combining the mean intensity values across the three channels.

$$\mathrm{NDVI}_{1064-532} = \frac{\overline{I}_{1064} - \overline{I}_{532}}{\overline{I}_{1064} + \overline{I}_{532}} \tag{13}$$

$$\mathrm{NDVI}_{1550-532} = \frac{\overline{I}_{1550} - \overline{I}_{532}}{\overline{I}_{1550} + \overline{I}_{532}} \tag{14}$$

$$\mathrm{NDVI}_{1550-1064} = \frac{\overline{I}_{1550} - \overline{I}_{1064}}{\overline{I}_{1550} + \overline{I}_{1064}} \tag{15}$$

Based on this set of LiDAR metrics, we tested five different sets of LiDAR

Table 4
Multispectral LiDAR metrics extracted for the sample plots*.

Metric	Description
Z_sd	Standard deviation of height distribution (m).
Z_skew	Skewness of height distribution.
Z_kurtosis	Kurtosis of height distribution.
Z_qP	*P*th height percentiles (m) (P = 25, 45, 75, and 95).
Z_pcumn	Cumulative percentage of returns in the *n*th of 10 equally spaced height intervals (%) (n = 1, 7, 9), where n = 1 refers to the lowest height interval.
vci	Vertical complexity index (van Ewijk et al., 2011).
ccmean	Mean crown closure: the number of 2 × 2 m canopy height model raster cells that have a height value greater or equal to the mean height canopy (%).
rumpleindex	Ratio of canopy surface to plot area (Kane et al., 2010).
cover2m	Percent of all returns above 2 m (%).
lad.cv	Coefficient of variation in the leaf area density (LAD) profile (m^2/m^2) (Bouvier et al., 2015).
I_tot	Sum of intensities.
I_max	Maximum intensity.
I_mean	Mean intensity.
I_sd	Standard deviation of intensity distribution.
I_cv	Coefficient of variation of intensity distribution.
I_skew	Skewness of intensity distribution.
I_kurtosis	Kurtosis of intensity distribution.
I_pcumzqP	Percentage of intensity returns below the *P*th height percentile (P = 10 to 90).
$NDVI_{1064-532}$	See Eq. (13).
$NDVI_{1550-532}$	See Eq. (14).
$NDVI_{1550-1064}$	See Eq. (15).

* height-derived metrics were only extracted from channel 2, whereas intensity-derived metrics were derived from channels 1, 2 and 3 and from the original and corrected intensity.

metrics as listed in the Table 5 for the prediction of three forest attributes, i.e., BA, QMD, and TPH. We performed all the calculations to derive the LiDAR metrics in R version 3.4.1 R Development Core Team (2015) using the lidR package version 1.5.0 (Roussel and Auty, 2018).

3.4. Plot level forest attribute predictions

In this study, we predicted forest attributes using the non-parametric modeling approach random forest (RF) (Breiman, 2001). This modeling approach consists of an ensemble of regression trees derived by bootstrapping (with replacement) both predictor variables and sample plot calibration data. The ensemble of regression trees can facilitate a progressive growth in order to yield a maximum predictive accuracy while at the same time the mechanism of bootstrapping tends to reduce the correlation between residuals of single trees (Breiman, 2001; Segal, 2003). RF models can handle complex, high-dimensional interactions between predictors and multicollinearity (Evans et al., 2011). In addition, RF models result in robust predictions due to its cross-validation during the model development phase (Penner et al., 2013). Lastly, wall-to-wall mapping of the forest attribute RF predictions at the landscape level is a relatively easy process (Immitzer et al., 2016). These RF model characteristics have made it one of the more frequently used approaches to predict LiDAR-based Forest Resource Inventory (FRI) attributes (White et al., 2017).

Table 5
Five sets of LiDAR metrics.

Metric	Description
Z_2	Normalized height-based LiDAR metrics from channel 2 (1064 nm)
ZIo_2	Normalized height-based and uncorrected intensity LiDAR metrics from channel 2 (1064 nm)
ZIc_2	Normalized height-based and corrected intensity LiDAR metrics from channel 2 (1064 nm)
ZIo_123	Normalized height-based LiDAR metrics from channel 2 (1064 nm), uncorrected intensity LiDAR metrics from channel 1 (1550 nm), 2 (1064 nm), and 3 (532 nm), and three NDVI metrics
ZIc_123	Normalized height-based LiDAR metrics from channel 2 (1064 nm); corrected intensity LiDAR metrics from channel 1 (1550 nm), 2 (1064 nm), and 3 (532 nm), and three NDVI metrics

Since the number of forest field plots was relatively low (i.e., 84 plots) in this study, the performance of the constructed forest models was examined based on the leave-one-out cross-validation (LOOCV) approach. The average bias and RMSE were computed to assess the performance of the RF models in both absolute and relative terms.

$$\text{bias} = \frac{1}{N}\sum_{i=1}^{N}(\hat{y}_i - y_i) \tag{16}$$

$$\%\text{bias} = \frac{\text{bias}}{\bar{y}} \times 100 \tag{17}$$

$$\text{RMSE} = \sqrt{\frac{1}{N}\sum_{i=1}^{N}(\hat{y}_i - y_i)^2} \tag{18}$$

$$\%\text{RMSE} = \frac{\text{RMSE}}{\bar{y}} \times 100 \tag{19}$$

where N is the number of validation plots, y_i is the observed value for plot i, $\hat{y}_i$ is the predicted value for plot i, and $\bar{y}$ is the mean of the observed attribute, i.e., BA, QMD, or TPH.

To compare the forest attribute observations with the five different RF predictions (i.e., the predictor sets: Z_2 to ZIc_123) we used regression-based equivalence tests (Robinson and Froese, 2004; Robinson et al., 2005). The bootstrapped two one-sided test (TOST) of equivalence examines the null hypothesis that the average difference between the intercept (β_0) and slope (β_1) for all forest attribute predictions and field observations are not equal to zero and one, respectively, i.e., the predictions are dissimilar from the observations in terms of intercept or slope or both. If the null hypothesis is rejected, the predictions are not significantly different from the observations (Robinson et al., 2005). The intercept component of the equivalence test is a measure of bias and determines if the mean of the observations is equivalent to the means of the model predictions. The slope component of the equivalence test is a measure of proportionality and determines if the slope between observations and model predictions is equivalent to one (Robinson et al., 2005; Fekety et al., 2018).

All statistical analyses were performed in R version 3.4.1 (R Development Core Team, 2015) using the caret package version 6.0–77 (Kuhn et al., 2008), randomForest version 4.6–12 (Liaw and Wiener, 2014) to predict forest attributes, and the equivalence package version 0.7.2 (Robinson, 2016) to perform equivalence tests between forest attribute predictions and observations. The script of Fekety et al. (2018) was used to produce equivalence tests graphical outputs.

4. Results

4.1. Removal of stripe artifacts in individual LiDAR flight lines by LSLC

Since channel 1 (1550 nm) and channel 2 (1064 nm) had notable stripe artifacts in their respective individual LiDAR flight lines, the LiDAR intensity data collected by these two channels were processed with LSLC. To assess and show the effects of stripe removal after implementing the LSLC we selected areas within individual flight lines that had different land cover types (forest, bare soil, roads, grassland, and wetland). Within the forest cover type we included natural/unmanaged and managed subtypes, including natural forest, plantation, shelterwood, and clearcut stands. Each land cover/forest cover type encompassed an area of approximately 90 m by 90 m (Figs. 3–5, and Tables 6 and 7). Apart from visual comparison, the effect of stripe removal can be quantitatively measured by computing the coefficient of

variation (*cv*). The *cv* is computed by dividing the standard deviation of the intensity by the mean of the intensity. A decrease of *cv* after LSLC implies a reduction of striping in intensity data, resulting in an improvement of intensity homogeneity. Table 6 shows the computed *cv* of the land cover before and after implementing the LSLC on the intensity data of channel 1 and channel 2. Fig. 3 shows the original intensity data and the LSLC intensity data for the four areas for channel 2 (1064 nm).

Based on the observation in Table 6 and Fig. 3, we can see that stripe artifacts caused by banding were successfully reduced in all land and forest cover types after implementing the LSLC. In all areas we observed a significant reduction of *cv*. For instance, in Area 1 (bare soil within a shelterwood stand), the *cv* of original intensity value of channels 1 and 2 were 0.084 and 0.199, respectively. A reduction of *cv* by 23.06% and 66.87% can be observed after implementing the LSLC. For a similar area (i.e., Area 3, a clearcut stand including plots with disturbed seed beds and natural regeneration) we recorded a similar *cv* reduction. The *cv* of original intensity was 0.211 in channel 1 and 0.232 in channel 2. After implementing the LSLC, the *cv* was reduced to 0.2 (↓5.09%) and 0.124 (↓46.5%), respectively, for channels 1 and 2. A similar degree of *cv* reduction can also be found in Area 4 (wetland). The percentage of *cv* reduction for channels 1 and 2 were 6.98% and 42.27%, respectively. Finally, Area 2 represents an open mixedwood natural forest stand in which the striping was not visually obvious. In addition, the *cv* reduction after implementing the LSLC was not as pronounced as in the previous three areas. A reduction of *cv* by 4.23 to 4.79% was achieved for both channels. The grassland in Area 2 also recorded a *cv* reduction by 0.19% in channel 1 and 36.03% in channel 2. For impervious surfaces, such as the road in Area 3, the LSLC was able to reduce the striping with a decrease of *cv* by approximately 7.78% and 39.8% in channels 1 and 2, respectively. Based on our analysis, the stripe artifacts appeared more obvious on hard ground objects (i.e., those possessing a unique intensity return). As a result, the effect of LSLC was more observable on bare soil, roads, and wetlands, whereas the improvement of intensity homogeneity in tree canopies was less obvious. Also, channel 2 suffered more serious intensity banding effects and striping than channel 1. Therefore, a higher *cv* reduction was recorded in channel 2 for all areas as a result of the successful removal of stripe artifacts.

4.2. Removal of stripe artifacts in overlapping LiDAR flight lines by LSLC and OIC

After implementing LSLC, the stripe artifacts in each individual LiDAR flight line were significantly reduced. However, mild levels of striping artifacts were still observed in the overlapping regions of the combined LiDAR flight lines. This can be attributed to the effect of range and angle, where longer range and larger incidence angle can induce a higher degree of attenuation of the backscattered laser signal. We selected four new sub-areas that encompassed the different land cover/forest types and that were located in the overlapping region of the LiDAR data strips to demonstrate the effect of implementing the OIC. Fig. 4 shows the original multispectral LiDAR intensity data and the LSLC and OIC intensity data for (i) a plantation (including a mature jack pine plantation, clearcut areas, natural regeneration, and a road); (ii) a dense mixedwood stand (mostly pine and poplar); (iii) a clearcut area (including plots with disturbed seed beds and natural regeneration); and (iv) a wetland.

To demonstrate the effect of radiometric correction near the swath edges, we selected a section of the overlapping LiDAR flight lines covering several land cover types, i.e., grassland, roads, and forest. A significant level of striping can be observed at the swath edge region in the original LiDAR data (Fig. 5a). After implementing the LSLC, most of the stripe artifacts were removed from individual LiDAR flight lines, leaving a mild level of noise at the swath edge. This is mainly due to the attenuation of the backscattered laser signal with long range and large incidence angle (Fig. 5b). Therefore, the OIC was subsequently implemented to remove most of the stripe artifacts at the swath edge (Fig. 5c).

Table 7 shows the computed *cv* of the three land cover classes found at the swath edge region. In channel 1, the *cv* of the original intensity within the grassland and forest cover types was 0.337 and 0.946, respectively. Both land cover types showed a reduction of *cv* by 2.1% after implementing the LSLC. A further reduction in *cv* by 12% and 5.51% was found after implementing the OIC for grassland and forest, respectively. In terms of roads, the *cv* of original intensity was 0.32. This value was reduced to 0.318 and 0.282, respectively, after applying the LSLC and OIC, resulting in a decrease of *cv* of 0.54% and 11.6%. In channel 2, the forest cover type showed the least *cv* reduction after

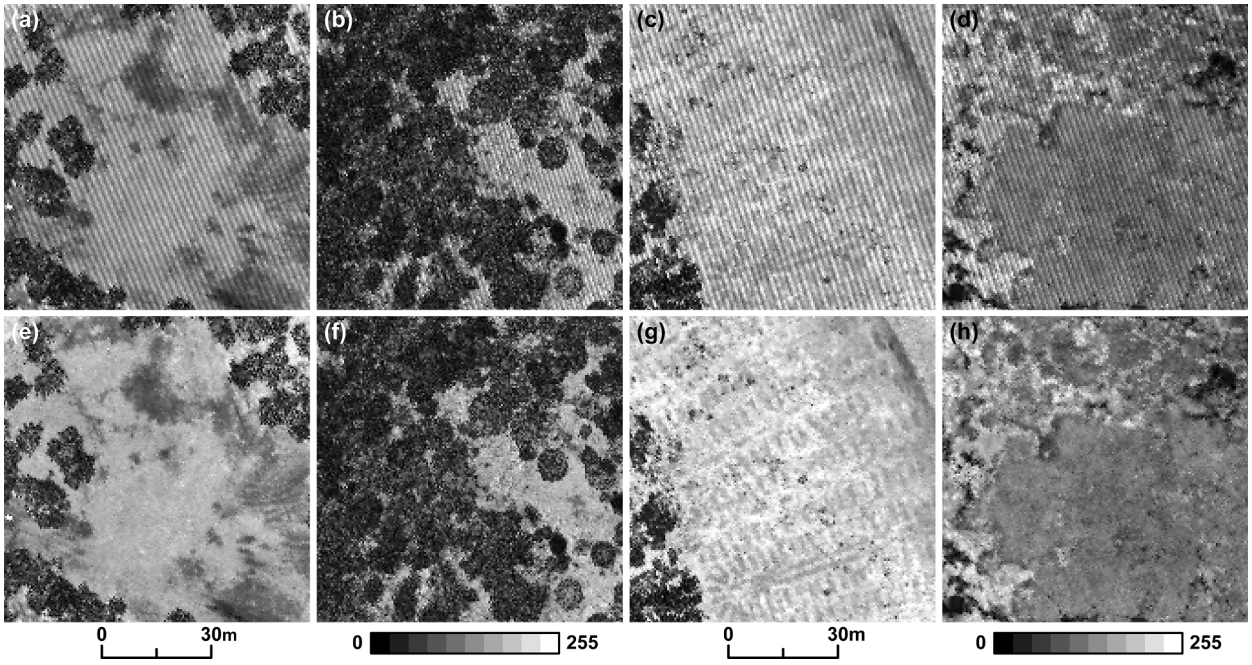

Fig. 3. (a) to (d) original intensity (channel 2, 1064 nm) data for Areas 1 to 4, and (e) to (h) LSLC intensity data for Areas 1 to 4. The striping caused by the intensity banding is obvious on the original intensity (a) to (d), and the LSLC successfully removes the striping.

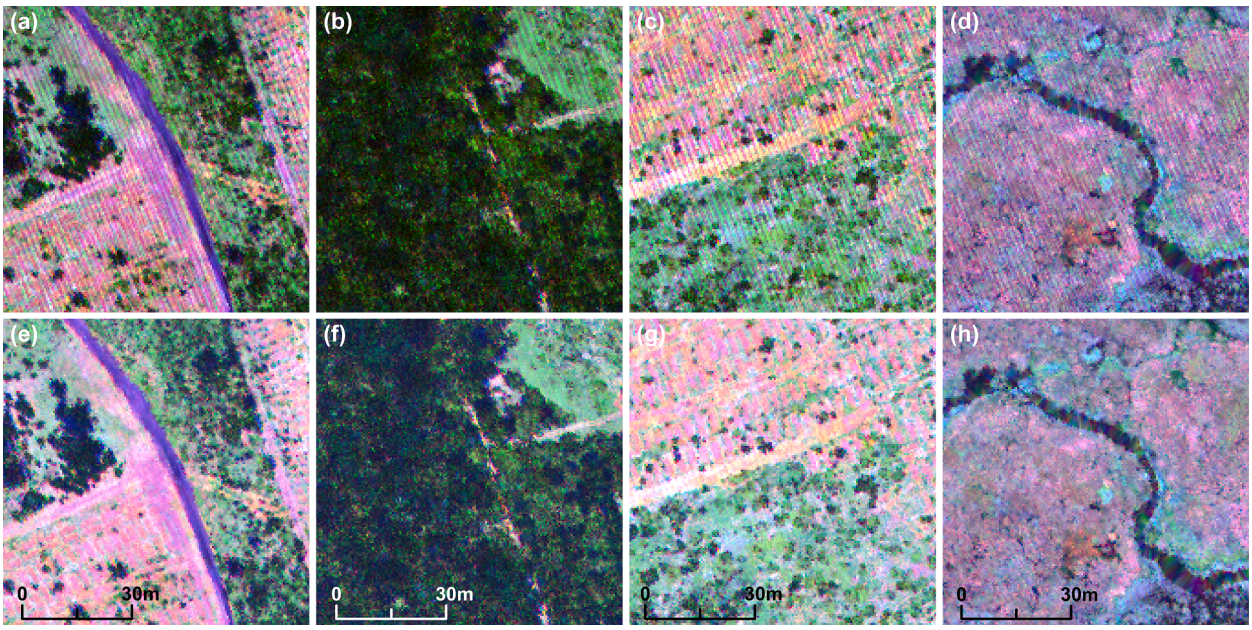

Fig. 4. (a) to (d) original multispectral LiDAR intensity data for the four sub-areas, and (e) to (h) LSLC and OIC multispectral LiDAR intensity data (Red: 1550 nm, Green: 1604 nm, Blue: 532 nm). (For interpretation of the references to colour in this figure legend, the reader is referred to the web version of this article.)

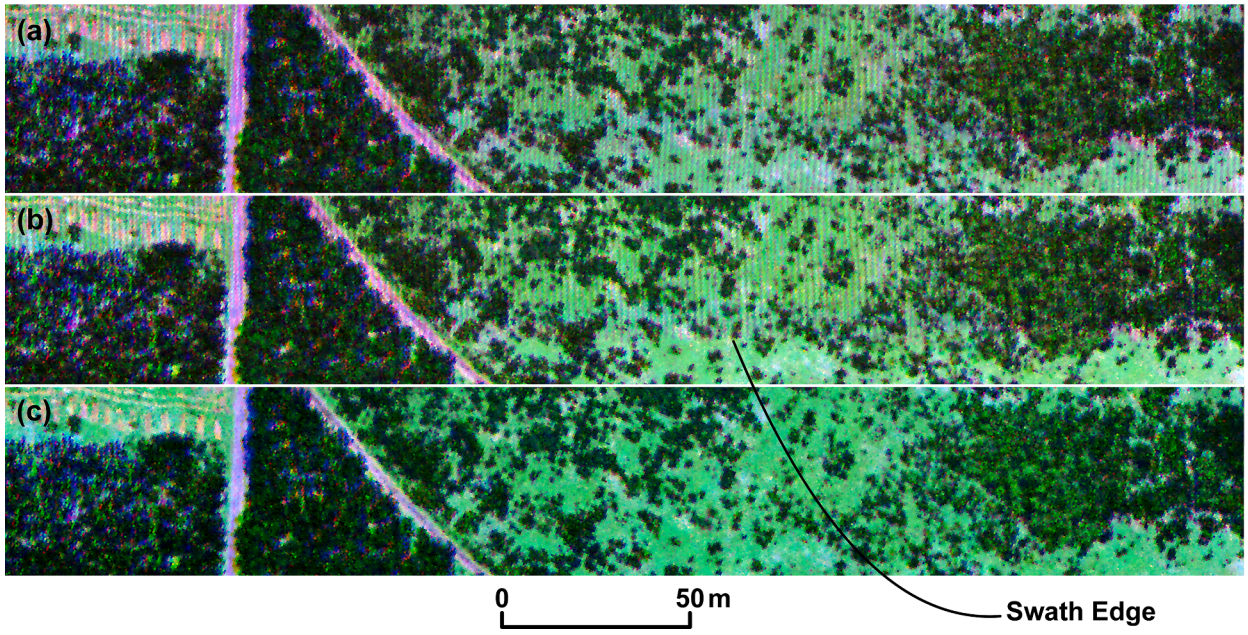

Fig. 5. A 50 m by 300 m sub-area in the PRF-site with two overlapping region combined by two strips: (a) Combined original LiDAR flight lines, (b) combined LiDAR flight lines after LSLC, and (c) combined LiDAR flight lines after LSLC and OIC (Red: 1550 nm, Green: 1604 nm, Blue: 532 nm). (For interpretation of the references to colour in this figure legend, the reader is referred to the web version of this article.)

implementing LSLC (↓2.54%) and OIC (↓6.37%). This reduction was similar to channel 1. Both the grassland (0.278) and paved road (0.295) had a low *cv* in the original intensity data. A decrease in *cv* of 14.19% and 6.78% was found after implementing the LSLC, and a further reduction of 42.93% and 31.43% after implementing the OIC for the respective two land cover types. Finally, in channel 3, we did not implement the LSLC since there was no intensity banding effect found in the individual LiDAR flight lines. Instead, we applied the OIC directly on the data, resulting in a reduction of *cv* by 33.77%, 11.05%, and 6.48%, respectively, for the grassland, road, and forest cover types.

4.3. Plot level forest attribute predictions

Prediction accuracy metrics (i.e., %RMSE and %Bias) for BA, QMD, and TPH are presented in Table 8 and scatterplots of the best BA, QMD, and TPH predictive models in Fig. 6. Although none of the five predictive models demonstrated a consistent model performance (in terms of %RMSE and %Bias) over the three forest attributes, some trends/tendencies can be observed. In terms of %RMSE, models including height and intensity metrics (models 2–5) performed better than predictive models that included only height metrics from channel 2 (i.e., model 1). %RMSE for BA and QMD improved by less than 2%, whereas the

Table 6
A comparison of *cv* between the original intensity and LSLC intensity.

	Channel 1 (1550 nm)		Channel 2 (1064 nm)	
	Original Intensity	LSLC intensity	Original Intensity	LSLC intensity
Area 1: Bare soil in shelterwood stand	0.084	0.065 (↓23.06%)	0.199	0.066 (↓66.87%)
Area 2: Open mixedwood natural forest stand	0.706	0.676 (↓4.23%)	0.650	0.619 (↓4.79%)
Area 2: Grassland	0.271	0.271 (↓0.19%)	0.261	0.167 (↓36.03%)
Area 3: Clearcut stand	0.211	0.200 (↓5.09%)	0.232	0.124 (↓46.5%)
Area 3: Road	0.166	0.153 (↓7.78%)	0.235	0.141 (↓39.8%)
Area 4: Wetland	0.247	0.230 (↓6.98%)	0.258	0.149 (↓42.27%)

improvement in %RMSE in TPH ranged from 3.5 to 7.2%. We did not observe any consistency, however, in terms of which of these four models (models 2–5), performed best in terms of %RMSE. For BA, model 3 (height and channel 2 corrected intensity) performed best (21.8% RMSE), for QMD, model 2 (height and channel 2 original intensity) performed best (23.3% RMSE), and for TPH, model 5 (height and corrected intensity from all three channels) performed best (35.3% RMSE). For QMD and TPH, %Bias decreased with the inclusion of intensity metrics, however, for BA we observed the opposite; i.e., %Bias increased by 0.1 to 0.3% compared to model 1 (channel 2 height metrics only). Again, the largest improvement in %Bias was observed in TPH (from 0.8 to 1.8%). RF's variable importance factor indicated that the two most important metrics for models 4 and 5 (height and intensity from all three channels) were $NDVI_{1550-1064}$ and $I\_kurtosis_{1550}$. Only the fourth ranked metric was a height-derived LiDAR metric, i.e., Z_pcum1, in these models. These results indicate that BA and QMD predictions in our study area gain relatively little from additional intensity metrics, in terms of using monochromatic versus multispectral metrics and in terms of correction of LiDAR intensity data. However, additional intensity metrics improve TPH predictions, especially when intensity metrics from multiple channels (i.e., multispectral LiDAR) and intensity NDVI metrics are included. Again, the application of a radiometric correction for modelling BA, QMD, and TPH resulted in minimal improvement (i.e., reduced RMSE or Bias).

The predictive models were further evaluated using statistical equivalence tests. Equivalence tests show that all five models for all three FRI attributes were statistically equivalent to the observed BA, QMD, and TPH in terms of bias, indicating that the means of the observations and predictions were equivalent at a ± 25% region of equivalence. However, in terms of proportionality (which tests if the slope between observation and predictions are equivalent to one), none of the model predictions were equivalent to the observed BA, QMD, and TPH at a ± 25% region of equivalence. The 95% confidence interval of the proportionality component extended outside of the lower range of the region of equivalence, indicating that all models, regardless whether intensity was included or excluded and regardless whether intensity was corrected or uncorrected, over predicted low BA, QMD, and TPH observations and under predicted high BA, QMD, and TPH observations.

We also evaluated the equivalence between prediction model 1 and models 2–5 (results not shown). BA and QMD model predictions, which included height and intensity metrics, were statistically equivalent to BA and QMD model predictions, which included height metrics only, both in terms of bias and proportionality. The results of these equivalence tests confirm the results of the prediction accuracy metrics (%RMSE and %Bias) (Table 8) that BA and QMD predictions in the PRF-site gained relatively little when intensity metrics were added to the variable predictor set for these attributes. Equivalence tests for TPH, on the other hand, indicated that TPH model 1 predictions (height metrics only) were not statistically equivalent to TPH models 2–5 predictions (height and intensity metrics). Hence, the inclusion of intensity metrics (original or corrected), especially multispectral intensity metrics, is more beneficial for the prediction of TPH.

5. Discussion

5.1. Removal of stripe artifacts by LSLC and OIC

The presence of stripe artifacts found in individual LiDAR flight lines and, after mosaicking, in overlapping flight lines, makes it necessary to implement radiometric pre-processing to improve the quality of the intensity data. Therefore, in this paper, we show that these errors should be addressed separately, starting with the individual LiDAR flight lines and subsequently the overlapping LiDAR data between adjacent flight lines.

The first type of stripe artifacts is attributed to the intensity banding effect, which is caused by the misalignment between the axes of the transmitted laser beam and the receiver's field of view (Yan and Shaker, 2018). The use of LSLC can significantly help remove these unwanted artifacts. Unless stripe artifacts are present in the LiDAR flight line, implementation of LSLC is optional. (for example, we did not implement

Table 8
BA, QMD, and TPH predictive RF model accuracies (%RMSE and %Bias) for the five predictor sets using LOOCV. The differences between model 1 (normalized height metrics only) and models 2–5 (including intensity metrics) are shown in brackets.

Model	BA		QMD		TPH	
	%RMSE	%Bias	%RMSE	%Bias	%RMSE	%Bias
1: z_2	23.7	**0.4**	25.1	-0.9	42.5	2.1
2: zIo_2	22.5 (↓1.2)	0.7 (↑0.3)	**23.3** **(↓1.8)**	-0.8 (↑0.1)	37.2 (↓5.3)	1.7 (↓0.4)
3: zIc_2	**21.8** **(↓1.9)**	0.5 (↑0.1)	24.9 (↓0.2)	-0.6 (↑0.3)	39.0 (↓3.5)	0.9 (↓1.2)
4: zIo_123	22.1 (↓1.6)	0.6 (↑0.2)	23.8 (↓1.3)	**−0.5** **(↑0.4)**	35.6 (↓6.9)	0.6 (↓1.5)
5: zIc_123	22.0 (↓1.7)	0.5 (↑0.1)	24.8 (↓0.3)	**−0.5** **(↑0.4)**	**35.3** **(↓7.2)**	**0.3** **(↓1.8)**

*Best models in terms of %RMSE and %Bias are indicated in bold.

Table 7
A comparison of *cv* between the original intensity, LSLC intensity and OIC intensity.

	Channel 1 (1550 nm)			Channel 2 (1064 nm)			Channel 3 (532 nm)		
	Original Intensity	LSLC Intensity	LSLC + OIC Intensity	Original Intensity	LSLC Intensity	LSLC + OIC Intensity	Original Intensity	LSLC Intensity	LSLC + OIC Intensity
Grassland	0.337	0.330 (↓2.11%)	0.297 (↓12.00%)	0.278	0.239 (↓14.19%)	0.159 (↓42.93%)	0.212	Nil	0.140 (↓33.77%)
Road	0.320	0.318 (↓0.54%)	0.282 (↓11.60%)	0.295	0.275 (↓6.78%)	0.203 (↓31.43%)	0.334	Nil	0.297 (↓11.05%)
Forest	0.946	0.925 (↓2.12%)	0.893 (↓5.51%)	0.706	0.688 (↓2.54%)	0.661 (↓6.37%)	0.403	Nil	0.377 (6.48%)

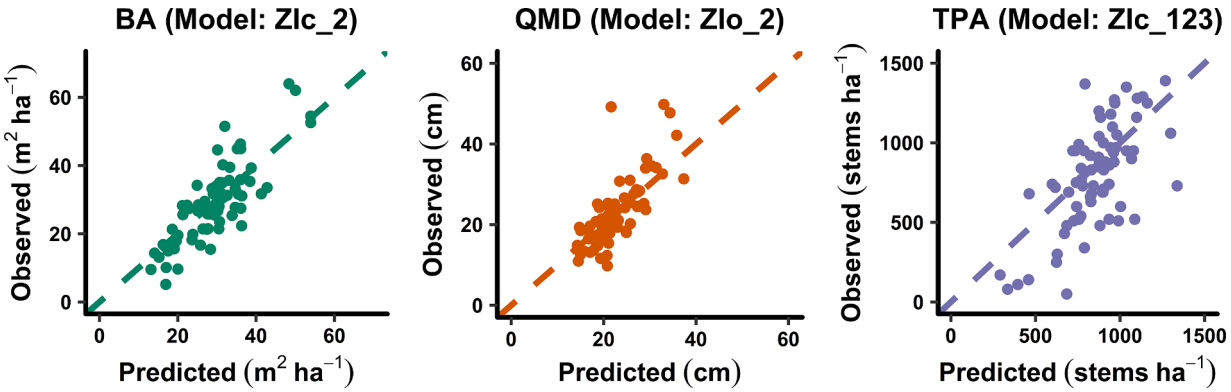

Fig. 6. FRI predictive models for BA, QMD, and TPH. Names in brackets indicate which of the five model results are shown and 1:1 lines are added to show the model's fit.

the LSLC on channel 3 in our case study). Also, these striping artifacts (or the intensity banding effect) tend to be more prevalent in the nadir region and less so towards the swath edges. This is mainly due to the speed of the oscillating mirror. When the oscillating mirror is operated at high speed, i.e., approaching the nadir region, the recorded laser beam may move away from the receiver's field of view, resulting in a significant laser energy loss in this particular scanning direction. On the other hand, when the oscillating mirror approaches the swath edge, the motion of the mirror decelerates, resulting in a high overlap factor between the laser beam and receiver's field of view. The *cv* computed in Table 4 refers to the land cover types collected at the close-to-nadir region, whereas the *cv* computed in Table 5 refers to the land cover types collected at the swath edge. For instance, in channel 2, the reduction of *cv* after implementing the LSLC was 36.03% for grassland at the close-to-nadir region, but the reduction of *cv* yielded only 14.19% if collected near the swath edge. Similarly, the computed *cv* for tree canopies was reduced by 5.09% and 2.54% for the LiDAR data points collected close to nadir and swath edge, respectively, after implementing the LSLC. Regarding the road feature, a notable difference can be observed between the value of *cv* reduction collected near nadir and at the swath edge, i.e., a percentage of reduction of 39.8% and 6.78% respectively. These numbers shed light on how the severity of stripe artifacts changes within different regions of the LiDAR flight line, and that the LSLC can successfully remove this noise regardless of its location.

The second type of stripe artifacts can be observed when combining two overlapping LiDAR flight lines. Although the stripe artifacts found in the individual LiDAR flight line is removed after LSLC, a low level of striping can be found at the swath edge of the overlapping LiDAR data. This can be attributed to the attenuation of laser energy due to the system and environmental induced distortions (mainly range and angle). Although there are several radiometric correction models based on the radar (range) equation to remove these effects, the degree of correction varies with respect to the study area and the system being used. Therefore, we utilize an overlap-driven approach to estimate the correction parameters, mainly for the range and angle. As shown here, the OIC successfully removed the stripe artifacts found in the swath edge. Comparisons among the three land cover types indicated that the *cv* for the forest cover type always recorded the least *cv* reduction after LSLC or LSLC and OIC. Since the laser footprint is larger than the individual components of the forest (i.e., tree stem, branches, and leaves), the signal is usually backscattered with multiple returns from these various components. Unlike those objects located on hard surfaces (e.g., grassland, bare ground, and road), the mechanism of laser energy attenuation in forests is harder to model. Therefore, the effect of radiometric correction on forests is not as obvious. In our study, this may explain why the forest attribute predictions using radiometrically corrected intensity metrics did not appear to be different from those predictive models using metrics derived from the original intensity data.

5.2. Plot level forest attribute predictions

Our results demonstrate that BA and QMD predictions in our study area gained relatively little from additional intensity metrics, both from monochromatic or multispectral LiDAR intensity data. Intensity metrics from multiple LiDAR channels and intensity NDVI metrics, did improve TPH predictions by up to 7.2 %RMSE and 1.8 %Bias. However, TPH prediction errors (%RMSE) were still approximately 10% larger than for BA and QMD. This indicates that stem density remains more difficult to predict, especially in structurally complex temperate forests like the PRF-site. All predictive models significantly over predicted low BA, QMD, and TPH observations and under predicted high BA, QMD, and TPH observations, regardless whether intensity (raw or corrected) was included or not and regardless whether monochromatic or multispectral LiDAR metrics were used. Our findings, in part, support previous studies that modeled plot-level forest attributes and compared the predictive performance of these models when LiDAR-derived height, intensity, or a combination were included (Hopkinson and Chasmer, 2009; García et al., 2010; Shang et al., 2017; van Ewijk et al., 2019). Hopkinson and Chasmer (2009) found that metrics derived from the LiDAR intensity data were more stable and less sensitive to canopy height, structural class, and sensor configuration than LiDAR height-derived metrics for modelling canopy fractional cover over seven study areas across Canada. García et al. (2010) found that models that included LiDAR derived height and intensity metrics or intensity metrics only resulted in a more accurate estimate of biomass in a mixed species Mediterranean forest than models based on height metrics alone. Those LiDAR intensity derived metrics incorporated at different height percentiles (i.e., can be treated as a combination of elevation and intensity information) along with intensity-based measures of canopy closure were chosen in their overall and species-specific biomass models. Shang et al. (2017) also showed that the combined use of height and intensity metrics gave more accurate predictions of size class specific stem densities in a temperate forest in Ontario, Canada compared to models including only height or intensity metrics. van Ewijk et al. (2019), compared BA, QMD, and TPH predictions at three Ontario forest sites and found, similar to this study, that at all three sites BA and QMD gained little in terms of prediction accuracy when intensity metrics were combined with height metrics derived from LiDAR data. However, TPH improvements in predictive accuracy varied by forest site, ranging from 0.6 to 6% improvements in %RMSE within their boreal and temperate forest sites, respectively.

In terms of comparing performance differences between the use of monochromatic and multispectral LiDAR derived metrics (height and intensity) in plot level forest attribute models, Dalponte et al. (2018) concluded that multispectral LiDAR models for above ground biomass, diameter variability, species diversity and stem density provided better prediction results than monochromatic LiDAR models (for a forest in southern Norway). They found that metrics derived from channel 1

(1550 nm) seemed the most useful for the forest attributes they modeled. Kukkonen et al. (2019a,b) also reported improvements for plot level predictions of dominant species, species proportions and volume (total and species-specific volume) for a boreal forest in eastern Finland when multispectral LiDAR metrics were used compared to monochromatic LiDAR metrics (i.e., Kappa improved from 0.74 (using monochromatic LiDAR metrics) to 0.81 (using multispectral LiDAR metrics) for their predictions of dominant tree species. The authors also reported that improvement of species-specific volume using multispectral LiDAR metrics was tree species dependent, with the largest %RMSE decrease found in broadleaved volumes (i.e., from 121.0 to 72.3 %RMSE) and the least in spruce volumes (i.e., 38.8 to 34.3 %RMSE). In our study, we only observed an improvement in performance accuracy of predictive models with multispectral LiDAR metrics (models 4 and 5) over predictive models using monochromatic LiDAR (models 2 and 3) for TPH but the difference between these models was small (<4 %RMSE). The differences in model performances between these studies may in part be explained by differences in forests (temperate versus boreal), by differences in forest attributes, and by differences in sampling design (e.g., stratification, plot size, and number of plots).

Most previous studies that have included intensity metrics to predict forest attributes (at the individual tree level, plot level, or classified land/forest cover types) have either used the original LiDAR intensity (Hopkinson et al., 2016; Shang et al., 2017; van Ewijk et al., 2019) or corrected/calibrated/normalized LiDAR intensity (García et al., 2010; Budei et al., 2018; Matikainen et al., 2017; Axelsson et al., 2018; Dalponte et al., 2018). Far fewer studies have performed a comparison to evaluate the effect of radiometric correction on forest attribute prediction outcomes (e.g., Korpela et al. (2010), Yan and Shaker (2014), Kukkonen et al. (2019a)). Korpela et al. (2010) found that individual species classification results improved when corrected LiDAR intensity metrics were used, regardless of classification approach (k-NN, LDA, and RF) for a forest in southern Finland. Yan and Shaker (2014) compared the overall accuracy of a land-cover classification in Burnaby, BC, Canada and found that radiometrically corrected and normalized intensity improved classification results up to 16.5% compared to using the original LiDAR intensity data. In both studies, the classification improvement was in part attributed to the improvement of the homogeneity of the intensity data during the radiometric correction process. Kukkonen et al. (2019a), on the other hand, concluded that their range correction of the LiDAR intensity data did not substantially improve the separation of boreal tree species at the plot level. Their range correction of the intensity data improved the classification accuracy (Kappa) of the dominant tree species only slightly (from 0.77 to 0.78). Since they only relied on the range correction without consideration of the angle effect, the mechanism of range correction did not have a significant difference regardless of using a correction parameter less than or equivalent to two. In this study, we further incorporated the angle correction (parameter b in Eq. (6)) and atmospheric correction (parameter c in Eq. (6)) and still observed the same tendency, i.e., differences in prediction accuracy of the plot level forest attributes are negligible when original intensity and corrected intensity metrics are used. In the section below we try to explain why the performance accuracy of our plot level forest attributes, unlike the performance of individual tree level attributes and land/forest cover classifications, show little difference when original and corrected intensity data (monochromatic or multispectral) are applied.

5.3. Effect of radiometric correction at different relevant spatial resolutions and its implications for modeling forest attributes

Our radiometric correction (i.e., LSLC and OIC) analyses demonstrate the reduction of stripe artifacts both in the individual LiDAR flight line and the combined overlapping LiDAR flight lines. The effect of this correction is clear when we generate LiDAR intensity images at fine scales (i.e., the intensity image resolution is equivalent or close to the mean point spacing). As a result, in this section, we aim to analyze the effect of radiometric correction at different spatial resolutions, which are relevant for the different types of forest attributes, i.e., individual tree attributes, plot level forest attributes, and land/forest cover types.

Although several studies have examined the effects of different spatial resolutions on the prediction of wall-to-wall forest attributes, especially for plot level attributes (Chen et al., 2016; Packalen et al., 2019), there is, as far as the authors are aware, a lack of research examining the effect of intensity noise found on the airborne LiDAR image with respect to different spatial resolutions. The original multispectral LiDAR intensity data and the radiometrically corrected multispectral LiDAR intensity image (after applying the LSLC and OIC) are presented in Fig. 7. At the finest spatial resolution, i.e., 0.5 m, striping was clearly visible in the original LiDAR intensity data, but was successfully removed in the radiometrically corrected data. The effect of striping was still notable on the original LiDAR intensity image with 1 m spatial resolution. However, at 2 m spatial resolution the effect of this noise was less obvious. When the resolution was further reduced (⩾5 m), there was no difference between the original and radiometrically corrected data. One can see that although the different land cover types (i.e., clearcut, natural regeneration, and pine plantation) can still be recognized on both sides of the road, the geometry of the road is hardly preserved at these broader spatial resolutions.

Based on our analysis, the effect of radiometric correction is notable when the multispectral airborne LiDAR intensity data are analyzed at its finest spatial resolution (i.e., 0.5 m in this case study). At this scale, the striping is obvious and they are completely removed after implementing the radiometric correction (i.e., LSLC and OIC). As a result, the effect of noise removal has a significant impact on applications, such as individual tree species classification (Korpela et al., 2010) and land-cover classification (Yan and Shaker, 2014), that require a fine-scale, high resolution data product. ABA plot sizes for the prediction of forest attributes typically range from 200 to 625 m^2, with the size of the largest trees often determining the plot size (White et al., 2017). These plot sizes are equivalent to ~15 m to 25 m spatial resolutions, at which the effect of radiometric correction on intensity metrics does not seem to have a significant effect. Here we have only shown the effect of spatial resolution changes on mean intensity. However, we expect that other LiDAR intensity metrics behave similarly.

The combination of sensitivity of LSLC and OIC to land cover type, i.e., we observed only minimal changes in intensity values after corrections in forest cover types compared to other land cover types (e.g., bare soils and roads), and the effect of spatial resolution on intensity noise may explain why we did not observe differences in plot level BA, QMD, and TPH prediction accuracies between models using uncorrected and corrected intensity data to the same extent as those that have been observed in studies at the ITC level and for land cover classifications (Korpela et al., 2010; Yan and Shaker, 2014). Further research is required to examine if our findings may be site and LiDAR sensor specific or if similar observations can be made under different forest conditions, with different LiDAR sensor specifications and acquisition parameters. The fact that the PRF-site is a structurally complex forest with a combination of natural and silviculturally treated stands, resulting in a varied set of forest structures that may also have contributed to the plot level forest attribute prediction results we observed.

6. Conclusions

Multispectral airborne LiDAR data have been recently introduced for the study of forest attributes; however the effect of radiometric correction on different cover types has not been fully examined. In this study, we proposed a two-stage radiometric correction to improve the quality of the multispectral airborne LiDAR intensity data collected by Optech Titan. The first process includes the use of the LSLC to reduce the intensity banding effect in the individual LiDAR flight lines. Second, we developed an OIC, which overcomes the drawback of existing radiometric correction methods that require hard thresholds for the model

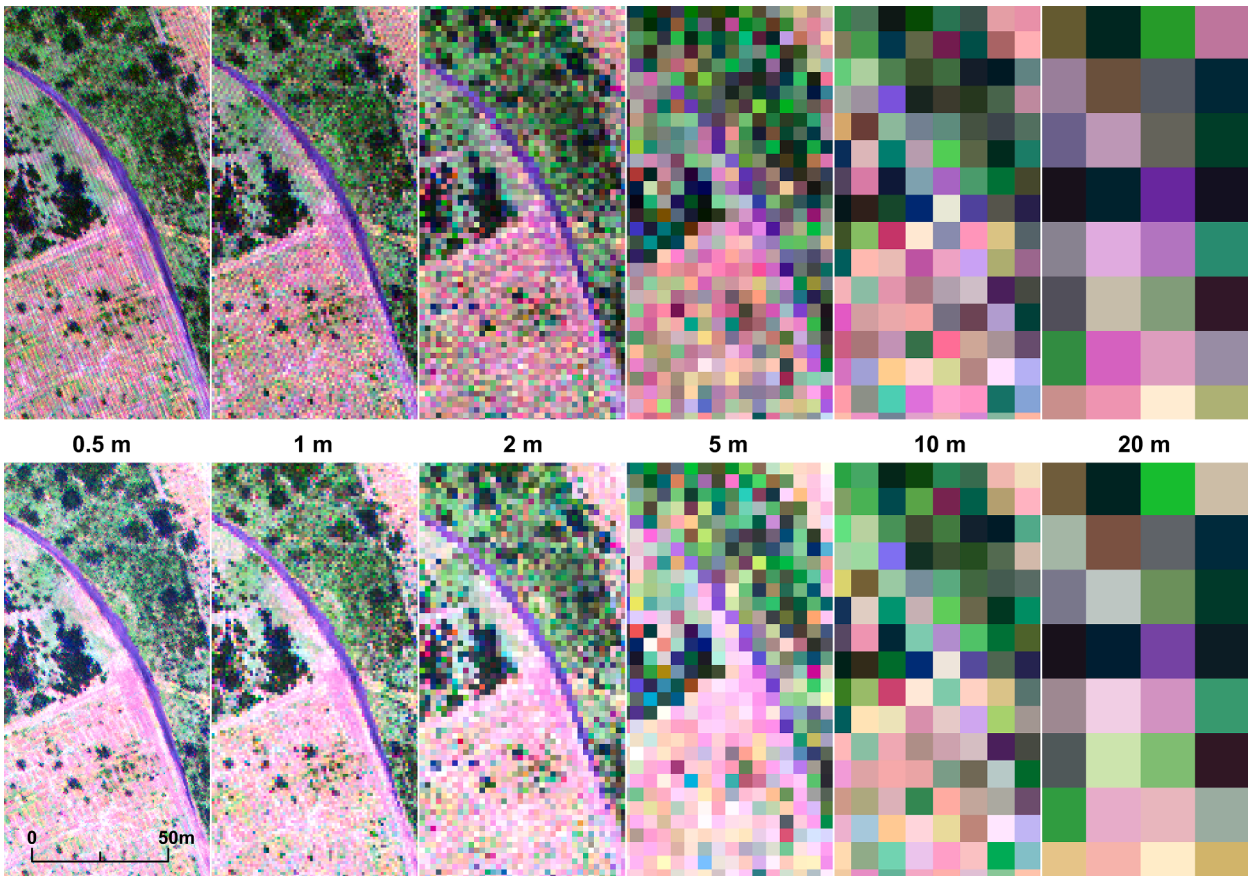

Fig. 7. Original intensity data at spatial resolutions ranging from 0.5 m to 20 m (upper row) and the radiometrically corrected intensity data (with both LSLC and OIC) at the corresponding spatial resolution (lower row).

parameters, to reduce striping found in the overlapping regions of combined LiDAR flight lines. In our study the impact of the LSLC was notable in the close-to-nadir region in channels 1 and 2, while the OIC aided in removing the stripe artifacts found at the overlapping regions of the combined LiDAR flight lines in all three channels. The combined corrections can yield to a reduction of *cv* by up to 12% in channel 1 (1550 nm), 42.93% in channel 2 (1064 nm), and 33.77% in channel 3 (532 nm).

Our forest attribute prediction results demonstrated that BA and QMD predictions improved relatively little with the additional LiDAR intensity metrics (either monochromatic or multispectral). We may draw the conclusion that these forest attributes, in our study site, are predominantly related to the structural composition (i.e., tree height) in forest stands, an aspect that is captured very well by the height-derived information within LiDAR data. On the other hand, TPH is a forest attribute that is often more difficult to predict using only the elevation of LiDAR point cloud data.

The use of metrics derived from corrected LiDAR intensity rather than original LiDAR intensity, did not improve plot level predictive accuracy of BA, QMD, and TPH, unlike studies that have used corrected intensity data for individual tree species and land/forest cover classification. In this study we have two explanations. First, there is variation in radiometric correction (i.e., LSLC and OIC) in different land cover types. LSLC and OIC seem to have a greater effect on hard surfaces (bare soil, roads and grass cover) than on permeable surfaces, such as tree canopies. Second, the effect of radiometric correction highly depends on the spatial resolution at which LiDAR intensity metrics are derived. At fine spatial resolutions (e.g., 0.5 m) the correction of intensity noise is notable. However, at broader spatial resolutions (e.g., 20 m) the effect of radiometric correction is no longer evident.

Implications of our findings for wall-to-wall forest attribute mapping in the context of forest monitoring and management are that although radiometric correction of LiDAR intensity is critical for improved ITC level tree species classification and land/forest cover type classification, it did not improve our plot level BA, QMD, and TPH predictions. Our results do not imply that radiometric correction of monochromatic or multispectral LiDAR intensity data is unnecessary for the prediction and wall-to-wall mapping of plot level forest attributes. However, at our forest site, no significant increase in prediction accuracy was observed when LiDAR metrics were derived from corrected versus uncorrected monochromatic or multispectral LiDAR intensity data.

Declaration of Competing Interest

The authors declare that they have no known competing financial interests or personal relationships that could have appeared to influence the work reported in this paper.

Acknowledgments

This research was in part funded by AWARE (Assessment of Wood Attributes from Remote Sensing NSERC CRDPJ462973-14; grantee Prof Nicholas Coops, UBC), in collaboration with the Canadian Wood Fibre Centre (CWFC), FP-Innovations and Tembec Incorporated. The research work of radiometric correction was funded by the Discovery Grant from the Natural Sciences and Engineering Research Council of Canada (NSERC) (RGPIN-2015–03960 and RGPIN-2020-05857), the FCE Start-up Fund of the Hong Kong Polytechnic University (BE2U), and the Early Career Scheme (Project Number: 25213320) by the Research Grants Council of the Hong Kong Special Administrative Region.

References

Axelsson, A., Lindberg, E., Olsson, H., 2018. Exploring multispectral ALS data for tree species classification. Remote Sens. 10 (2), 183.

Bakuła, K., Kupidura, P., Jełowicki, Ł., 2016. Testing of land cover classification from multispectral airborne laser scanning data. Int. Arch. Photogram., Remote Sens. Spatial Inform. Sci. 41, 161–169.

Bouvier, M., Durrieu, S., Fournier, R.A., Renaud, J.-P., 2015. Generalizing predictive models of forest inventory attributes using an area-based approach with airborne LiDAR data. Remote Sens. Environ. 156, 322–334.

Brandtberg, T., 2007. Classifying individual tree species under leaf-off and leaf-on conditions using airborne lidar. ISPRS J. Photogram. Remote Sens. 61 (5), 325–340.

Breiman, L., 2001. Random forests. Mach. Learn. 45 (1), 5–32.

Budei, B.C., St-Onge, B., Hopkinson, C., Audet, F.-A., 2018. Identifying the genus or species of individual trees using a three-wavelength airborne lidar system. Remote Sens. Environ. 204, 632–647.

Carleton, T., 2003. Old growth in the great lakes forest. Environ. Rev. 11 (S1), S115–S134.

Charaniya, A.P., Manduchi, R., Lodha, S.K., 2004. Supervised parametric classification of aerial lidar data. In: 2004 Conference on Computer Vision and Pattern Recognition Workshop. IEEE, p. 30.

Chen, Q., McRoberts, R.E., Wang, C., Radtke, P.J., 2016. Forest aboveground biomass mapping and estimation across multiple spatial scales using model-based inference. Remote Sens. Environ. 184, 350–360.

Chen, Y., Su, W., Li, J., Sun, Z., 2009. Hierarchical object oriented classification using very high resolution imagery and LiDAR data over urban areas. Adv. Space Res. 43 (7), 1101–1110.

Dalponte, M., Bruzzone, L., Gianelle, D., 2012. Tree species classification in the Southern Alps based on the fusion of very high geometrical resolution multispectral/hyperspectral images and LiDAR data. Remote Sens. Environ. 123, 258–270.

Dalponte, M., Ene, L., Gobakken, T., Næsset, E., Gianelle, D., 2018. Predicting selected forest stand characteristics with multispectral ALS data. Remote Sens. 10 (4), 586.

Ding, Q., Chen, W., King, B., Liu, Y., Liu, G., 2013. Combination of overlap-driven adjustment and Phong model for LiDAR intensity correction. ISPRS J. Photogram. Remote Sens. 75, 40–47.

Evans, J.S., Murphy, M.A., Holden, Z.A., Cushman, S.A., 2011. Modeling species distribution and change using random forest. In: Predictive species and habitat modeling in landscape ecology. Springer, pp. 139–159.

Fekety, P.A., Falkowski, M.J., Hudak, A.T., Jain, T.B., Evans, J.S., 2018. Transferability of lidar-derived basal area and stem density models within a Northern Idaho Ecoregion. Canad. J. Remote Sens. 44 (2), 131–143.

Fernandez-Diaz, J.C., Carter, W.E., Glennie, C., Shrestha, R.L., Pan, Z., Ekhtari, N., Singhania, A., Hauser, D., Sartori, M., 2016. Capability assessment and performance metrics for the Titan multispectral mapping lidar. Remote Sens. 8 (11), 936.

García, M., Riaño, D., Chuvieco, E., Danson, F.M., 2010. Estimating biomass carbon stocks for a Mediterranean forest in central Spain using LiDAR height and intensity data. Remote Sens. Environ. 114 (4), 816–830.

Gatziolis, D., 2011. Dynamic range-based intensity normalization for airborne, discrete return lidar data of forest canopies. Photogram. Eng. Remote Sens. 77 (3), 251–259.

Guo, L., Chehata, N., Mallet, C., Boukir, S., 2011. Relevance of airborne lidar and multispectral image data for urban scene classification using random forests. ISPRS J. Photogram. Remote Sens. 66 (1), 56–66.

Höfle, B., Pfeifer, N., 2007. Correction of laser scanning intensity data: Data and model-driven approaches. ISPRS J. Photogram. Remote Sens. 62 (6), 415–433.

Hopkinson, C., 2007. The influence of flying altitude, beam divergence, and pulse repetition frequency on laser pulse return intensity and canopy frequency distribution. Canad. J. Remote Sens. 33 (4), 312–324.

Hopkinson, C., Chasmer, L., 2009. Testing lidar models of fractional cover across multiple forest ecozones. Remote Sens. Environ. 113 (1), 275–288.

Hopkinson, C., Chasmer, L., Gynan, C., Mahoney, C., Sitar, M., 2016. Multisensor and multispectral LiDAR characterization and classification of a forest environment. Canad. J. Remote Sens. 42 (5), 501–520.

Im, J., Jensen, J.R., Hodgson, M.E., 2008. Object-based land cover classification using high-posting-density LiDAR data. GIScience & Remote Sens. 45 (2), 209–228.

Immitzer, M., Stepper, C., Böck, S., Straub, C., Atzberger, C., 2016. Use of worldview-2 stereo imagery and national forest inventory data for wall-to-wall mapping of growing stock. For. Ecol. Manage. 359, 232–246.

Jelalian, A.V., 1992. Laser radar systems. Artech House.

Jutzi, B., Gross, H., 2010. Investigations on surface reflection models for intensity normalization in airborne laser scanning (ALS) data. Photogram. Eng. Remote Sens. 76 (9), 1051–1060.

Kandare, K., Dalponte, M., Ørka, H., Frizzera, L., Næsset, E., 2017. Prediction of species-specific volume using different inventory approaches by fusing airborne laser scanning and hyperspectral data. Remote Sens. 9 (5), 400.

Kane, V.R., Bakker, J.D., McGaughey, R.J., Lutz, J.A., Gersonde, R.F., Franklin, J.F., 2010. Examining conifer canopy structural complexity across forest ages and elevations with LiDAR data. Can. J. For. Res. 40 (4), 774–787.

Kim, S., Hinckley, T., Briggs, D., 2011. Classifying individual tree genera using stepwise cluster analysis based on height and intensity metrics derived from airborne laser scanner data. Remote Sens. Environ. 115 (12), 3329–3342.

Korpela, I., Ørka, H.O., Hyyppä, J., Heikkinen, V., Tokola, T., 2010. Range and AGC normalization in airborne discrete-return LiDAR intensity data for forest canopies. ISPRS J. Photogram. Remote Sens. 65 (4), 369–379.

Kuhn, M., et al., 2008. Building predictive models in R using the caret package. J. Stat. Softw. 28 (5), 1–26.

Kukkonen, M., Maltamo, M., Korhonen, L., Packalen, P., 2019a. Multispectral airborne LiDAR data in the prediction of boreal tree species composition. IEEE Trans. Geosci. Remote Sens. 57 (6), 3462–3471.

Kukkonen, M., Maltamo, M., Korhonen, L., Packalen, P., 2019b. Comparison of multispectral airborne laser scanning and stereo matching of aerial images as a single sensor solution to forest inventories by tree species. Remote Sens. Environ. 231, 111208.

Lefsky, M.A., Cohen, W., Acker, S., Parker, G.G., Spies, T., Harding, D., 1999. Lidar remote sensing of the canopy structure and biophysical properties of douglas-fir western hemlock forests. Remote Sens. Environ. 70 (3), 339–361.

Liaw, A., Wiener, M., 2014. randomForest: Breiman and Cutler's Random Forests for Classification and Regression. http://cran.r-project.org/package=randomForest, accessed: August 1, 2018.

Lim, K., Treitz, P., Wulder, M., St-Onge, B., Flood, M., 2003. LiDAR remote sensing of forest structure. Prog. Phys. Geogr. 27 (1), 88–106.

Matikainen, L., Karila, K., Hyyppä, J., Litkey, P., Puttonen, E., Ahokas, E., 2017. Object-based analysis of multispectral airborne laser scanner data for land cover classification and map updating. ISPRS J. Photogram. Remote Sens. 128, 298–313.

Morsdorf, F., Mårell, A., Koetz, B., Cassagne, N., Pimont, F., Rigolot, E., Allgöwer, B., 2010. Discrimination of vegetation strata in a multi-layered mediterranean forest ecosystem using height and intensity information derived from airborne laser scanning. Remote Sens. Environ. 114 (7), 1403–1415.

Morsdorf, F., Nichol, C., Malthus, T., Woodhouse, I.H., 2009. Assessing forest structural and physiological information content of multi-spectral LiDAR waveforms by radiative transfer modelling. Remote Sens. Environ. 113 (10), 2152–2163.

Morsy, S., Shaker, A., El-Rabbany, A., 2017. Multispectral LiDAR data for land cover classification of urban areas. Sensors 17 (5), 958.

Næsset, E., 2007. Airborne laser scanning as a method in operational forest inventory: Status of accuracy assessments accomplished in scandinavia. Scand. J. For. Res. 22 (5), 433–442.

Næsset, E., Gobakken, T., Holmgren, J., Hyyppä, H., Hyyppä, J., Maltamo, M., Nilsson, M., Olsson, H., Persson, Å., Söderman, U., 2004. Laser scanning of forest resources: the nordic experience. Scand. J. For. Res. 19 (6), 482–499.

Ørka, H., Næsset, E., Bollandsas, O., 2009. Comparing classification strategies for tree species recognition using airborne laser scanner data. Proceedings of SilviLaser 2009, 46–53.

Packalen, P., Strunk, J., Packalen, T., Maltamo, M., Mehtätalo, L., 2019. Resolution dependence in an area-based approach to forest inventory with airborne laser scanning. Remote Sens. Environ. 224, 192–201.

Penner, M., Pitt, D., Woods, M., 2013. Parametric vs. nonparametric LiDAR models for operational forest inventory in boreal Ontario. Canad. J. Remote Sens. 39 (5), 426–443.

Penner, M., Woods, M., 2015. LiDAR Stand-Level Predictions for the PRF. Ontario Ministry of Natural Resources and Forestry, Peterborough, ON, Canada (Unpublished Work).

Poullain, E., Garestier, F., Levoy, F., Bretel, P., 2016. Analysis of ALS intensity behavior as a function of the incidence angle in coastal environments. IEEE J. Select. Top. Appl. Earth Observ. Remote Sens. 9 (1), 313–325.

R Development Core Team, 2015. R: A language and environment for statistical computing.

Robinson, A., 2016. Equivalence: Provides Tests and Graphics for Assessing Tests of equivalence. R package version 0.7.2. https://CRAN.R-project.org/package=equivalence, accessed: August 1, 2018.

Robinson, A.P., Duursma, R.A., Marshall, J.D., 2005. A regression-based equivalence test for model validation: shifting the burden of proof. Tree Physiol. 25 (7), 903–913.

Robinson, A.P., Froese, R.E., 2004. Model validation using equivalence tests. Ecol. Model. 176 (3–4), 349–358.

Roussel, J., Auty, D., 2018. lidr: Airborne lidar data manipulations and visualisation for forestry applications. http://cran.r-project.org/package=lidR, accessed: August 1, 2018.

Segal, M., 2003. Machine Learning Benchmarks and Random Forest Regression. Center for Bioinformatics and Molecular Biostatistics, UCSF: San Francisco, CA, USA.

Shang, C., Treitz, P., Caspersen, J., Jones, T., 2017. Estimating stem diameter distributions in a management context for a tolerant hardwood forest using ALS height and intensity data. Canad. J. Remote Sens. 43 (1), 79–94.

Tan, K., Cheng, X., 2017. Specular reflection effects elimination in terrestrial laser scanning intensity data using phong model. Remote Sens. 9 (8), 853.

van Ewijk, K., Treitz, P., Woods, M., Jones, T., Caspersen, J., 2019. Forest site and type variability in ALS-based forest resource inventory attribute predictions over three Ontario forest sites. Forests 10 (3), 226.

van Ewijk, K.Y., Treitz, P.M., Scott, N.A., 2011. Characterizing forest succession in Central Ontario using LiDAR-derived indices. Photogram. Eng. Remote Sens. 77 (3), 261–269.

Vierling, K.T., Vierling, L.A., Gould, W.A., Martinuzzi, S., Clawges, R.M., 2008. Lidar: shedding new light on habitat characterization and modeling. Front. Ecol. Environ. 6 (2), 90–98.

Watkins, L., 2011. The forest resources of Ontario 2011. Sault Ste. Ontario Ministry of Natural Resources, Marie (Ontario).

White, J., Tompalski, P., Vastaranta, M., Wulder, M.A., Saarinen, N., Stepper, C., Coops, N.C., et al., 2017. A model development and application guide for generating an enhanced forest inventory using airborne laser scanning data and an area-based approach. Ressources naturelles Canada, Natural Resources Canada.

Woods, M., Lim, K., Treitz, P., 2008. Predicting forest stand variables from LIDAR data in the Great Lakes St. Lawrence Forest of Ontario. Forest. Chronicle 84 (6), 827–839.

Woods, M., Pitt, D., Penner, M., Lim, K., Nesbitt, D., Etheridge, D., Treitz, P., 2011. Operational implementation of a LiDAR inventory in Boreal Ontario. Forest. Chronicle 87 (4), 512–528.
Wulder, M.A., Coops, N.C., Hudak, A.T., Morsdorf, F., Nelson, R., Newnham, G., Vastaranta, M., 2013. Status and prospects for LiDAR remote sensing of forested ecosystems. Canad. J. Remote Sens. 39 (sup1), S1–S5.
Yan, W.Y., Shaker, A., 2014. Radiometric correction and normalization of airborne LiDAR intensity data for improving land-cover classification. IEEE Trans. Geosci. Remote Sens. 52 (12), 7658–7673.
Yan, W.Y., Shaker, A., 2018. Airborne LiDAR intensity banding: Cause and solution. ISPRS J. Photogram. Remote Sens. 142, 301–310.
Yan, W.Y., Shaker, A., El-Ashmawy, N., 2015. Urban land cover classification using airborne LiDAR data: A review. Remote Sens. Environ. 158, 295–310.
Yu, X., Hyyppä, J., Litkey, P., Kaartinen, H., Vastaranta, M., Holopainen, M., 2017. Single-sensor solution to tree species classification using multispectral airborne laser scanning. Remote Sens. 9 (2), 108.
Zhang, K., Yan, J., Chen, S.-C., 2006. Automatic construction of building footprints from airborne LIDAR data. IEEE Trans. Geosci. Remote Sens. 44 (9), 2523–2533.